Supplementary Materials for

Observing the evolution of the Sun's global coronal magnetic field over 8 months

Zihao Yang *et al*.

Corresponding author: Hui Tian, huitian@pku.edu.cn

Science **386**, 76 (2024)
DOI: 10.1126/science.ado2993

The PDF file includes:

Materials and Methods
Supplementary Text
Figs. S1 to S4
Table S1
References

Other Supplementary Material for this manuscript includes the following:

Movies S1 to S3

1. Materials and Methods

1.1 Observations and Models

1.1.1 Upgraded Coronal Multi-channel Polarimeter (UCoMP)

We used data obtained with the UCoMP instrument from 19 February 2022 to 29 October 2022. A total of 114 observations (Table S1) were used to derive the global maps of coronal magnetic field. Compared to CoMP, UCoMP has a larger field-of-view (FOV) ranging from ~1.05 to ~1.6 solar radii (this refers to the FOV that can usually be used for coronal magnetic field diagnostics; the FOV recorded on the detector extends from ~1.05 to 2 solar radii in the east-west direction and from ~1.05 to ~1.6 solar radii in the north-south direction) and a slightly higher spatial resolution of ~6″. UCoMP observes a range of spectral lines which are sensitive to plasma at different temperatures; we used the intensity profiles of the two infrared Fe XIII lines at 1074.7 nm and 1079.8 nm.

For each observation set, a sequence of continuous Fe XIII 1074.7 nm intensity images at three different wavelength positions (1074.59 nm, 1074.70 nm and 1074.81 nm) were used to determine the wave parameters. The data used for wave tracking consists of approximately 120 frames (varies for different datasets, see Table S1) with a time cadence of ~33.5 s. These images were first coaligned. For each time step, we then fitted a Gaussian function to the three-point line profile for every pixel within the FOV, to determine the line parameters: peak intensity, Doppler velocity (relative to the rest wavelength) and line width (*24*). To correct an apparent east-west trend in the Doppler velocity, a polynomial function was fitted to the variation of the mean Doppler velocity in the east-west direction, then subtracted from the values (*24*). We also identified a time-dependent variation in the mean Doppler velocity throughout the continuous observation on each day. To correct for this trend, a linear function was fitted to the time series of the mean Doppler velocity, then also subtracted from the data. Fig. S1 shows an example of the two corrections.

An additional set of nearly simultaneous Fe XIII 1074.7 nm and 1079.8 nm intensity images were used to perform density diagnostics. This series of intensity data was observed several tens of minutes before the wave observations. For each spectral line, multiple frames (typically 4, varying for different datasets, see Table S1) of intensity images at each wavelength position (for the Fe XIII 1074.7 nm line: 1074.59 nm, 1074.70 nm and 1074.81 nm; for the Fe XIII 1079.8 nm line: 1079.69 nm, 1079.80 nm and 1079.91 nm) were coaligned and averaged to enhance the signal-to-noise ratio (S/N). These images were also coaligned to the Doppler velocity images.

We only performed analysis for coronal regions with sufficient S/N, determined as regions where the Fe XIII 1074.7 nm intensity exceeds 1.8 parts per million (ppm) of the intensity on the solar disk.

1.1.2 Solar UltraViolet Imager (SUVI)

We used archival extreme-ultraviolet (EUV) imaging observations from the SUVI instrument on the GOES spacecraft. SUVI provides coronal EUV images with a FOV that matches the FOV of UCoMP.

Figure 1 shows the SUVI level-2 composite images from the GOES archive, which are high-dynamic-range images generated from multiple exposures with short and long integration times. These composite images were observed using the 19.5 nm channel of SUVI with a spatial pixel size of 2.5″. Fig. 1, A, D and G used observations taken from 19:48 UT to 19:52 UT on 21 February 2022, from 20:48 UT to 20:52 UT on 1 June 2022 and from 19:48 UT to 19:52 UT on 5 August 2022, respectively.

1.1.3 Helioseismic and Magnetic Imager (HMI)

To compare with our synoptic coronal magnetic field maps (Carrington maps of the coronal magnetic field), we used archival HMI synoptic photospheric magnetograms (radial component) spanning several Carrington rotations from CR2254 to CR2263. Each synoptic magnetogram was constructed from HMI 720-s line-of-sight full-disk magnetograms. Initially, the 720-s line-of-sight magnetograms were converted to radial magnetograms. Then the magnetograms were interpolated onto a Carrington coordinate system. For each Carrington longitude, the magnetic field values were obtained by averaging the values from magnetograms with central meridians in close proximity to the corresponding Carrington longitude. The final product of the synoptic magnetogram combines HMI 720-s disk magnetograms over a full solar rotation (~27.27 days) and has original dimensions of 3600 pixels $\times$ 1440 pixels. For the three examples in Fig. 4, we used HMI synoptic magnetograms from CR2254, CR2258 and CR2260 as the boundary condition for coronal MHD models. A boundary magnetogram has approximately 300×144 mesh points in the $\phi - \theta$ directions. Here ϕ and θ refer to the azimuthal and polar angles, respectively. A uniform grid in the ϕ direction and a slightly non-uniform grid in the θ direction were employed. The resolution in the θ direction is matched to that in ϕ at the equator, and is slightly coarser towards higher latitudes. The pixel size at the equator of the boundary magnetogram is approximately $0.021\ \mathrm{R_s} \times 0.021\ \mathrm{R_s}$.

1.1.4 Magnetohydrodynamic model

For comparison with the observations, we used the Magnetohydrodynamic Algorithm outside a Sphere (MAS) model, from Predictive Science, which is a 3D MHD model of the thermodynamics and magnetic structure of the solar corona (*34*). A detailed description of the MAS model setup has been published previously (*37*). The MAS model solves resistive MHD equations including thermal conduction, radiative loss and coronal heating terms. The boundary condition for the model is the synoptic photospheric magnetogram (radial component) derived from HMI observations. We used MAS models generated using the synoptic photospheric magnetograms from CR2254, CR2258 and CR2260 as the boundary conditions.

The models have dimensions of 255×144×300 (r, θ, ϕ), with the radial distance (r) ranging from 1 to 30 solar radii. The model grid is uniform in the ϕ direction and slightly non-uniform in the θ direction. The voxel size in the $\phi - \theta$ directions at the equator is approximately $0.021\, r \times 0.021\, r$, where r is the distance from solar center. We adopted the empirical thermodynamic heating model 2 in the MAS code, similar to the one used in previous work (*34,* the third heating model). This heating model accounts for different heating functions with varying heating rates for active regions, quiet-Sun regions and coronal holes (*34, 38*).

Previous studies often applied a factor of 1.4 to correct the radial component of the photospheric magnetic field from HMI measurements before using them as input for MAS models. Those studies included this factor to account for differences between measurements from HMI and the Michelson Doppler Imager (MDI) (*39*) on the Solar and Heliospheric Observatory (*40*), and was used for MAS models calculated while MDI was operating (*33*). To maintain consistency with previous works, we also multiplied the HMI photospheric magnetograms by a factor of 1.4 before running the MAS models for the three Carrington rotations.

The MAS model output provides three-dimensional distributions of the coronal magnetic field vector, density and temperature in a spherical coordinate system. From these model outputs, we calculated the coronal emissivity and POS component of the magnetic field strength and direction along each line-of-sight (LOS) using Equation 2. The results are shown in Figure 4.

1.1.5 Potential Field Source Surface (PFSS) model

We also used the PFSS model for comparison. This is also a coronal magnetic field model using the synoptic photospheric magnetogram as the boundary condition. It extrapolates the magnetic field into the corona under the assumption of a potential field, containing no current or magnetic free energy. We used a PFSS model extrapolated from the synoptic photospheric magnetogram sampled at 18:03:28 UT on 21 February, 2022.

1.1.6 Atomic data

We adopted atomic data from the CHIANTI database version 10.0 (*41, 42*). For our calculation, the spontaneous radiative decay rates and the electron collisional rates of Fe XIII ions (*43*) implemented in the CHIANTI database were used.

1.1.7 Synthetic observables

We used the FORWARD software package implemented within the SOLARSOFT framework (*44*). Using FORWARD, we obtained the POS component of the coronal magnetic field along each LOS from the MAS models and investigated the LOS integration effect. We also synthesized the emissivity of the Fe XIII 1074.7 nm line along each LOS using FORWARD. The model magnetic field and the synthesized emissivity were combined to derive the LOS emissivity-weighted coronal magnetic field strength and direction using Equation 2. The POS component of the coronal magnetic field on the POS crossing solar center and perpendicular to the LOS was also obtained from the PFSS model using FORWARD.

1.2 Methods

1.2.1 Derivation of the wave phase speed

Previous studies showed that the prevalent transverse waves observed with CoMP and UCoMP are kink waves (*17, 19, 21*). In the corona, where the lengths of magnetic flux tubes are generally

much larger than the radii of their cross sections (known as the long-wavelength limit or thin flux-tube approximation), the phase speed of kink waves in cylindrical flux tubes can be approximated as

$$v_k \approx \sqrt{\frac{B_{\mathrm{n}}^2+B_{\mathrm{x}}^2}{\mu_0(\rho_{\mathrm{n}}+\rho_{\mathrm{x}})}} \qquad \text{(S1)}$$

which relates the kink speed in a coronal flux tube to the magnetic field ($B_{\mathrm{n,x}}$) and density ($\rho_{\mathrm{n,x}}$) in the interior (denoted by subscript n) and exterior (denoted by subscript x) of the flux tube. At the coronal heights observed by UCoMP, the coronal plasma-β (the ratio between gas pressure and magnetic pressure) is typically $\ll 1$. In such an environment, the pressure balance between the interior and exterior of a flux tube requires $B_{\mathrm{n}} \sim B_{\mathrm{x}}$ (*17, 45, 46*). In addition, the widths of coronal flux tubes (*47*) are usually much smaller than the spatial resolution (~6″) of UCoMP, so we assumed that the observations do not resolve individual flux tubes.

The observed emission in each pixel originates from both regions inside and outside flux tubes. Because the observed infrared line emission is contributed by both collisional excitation (line intensity proportional to the square of electron density N_e^2) and photo-excitation (line intensity proportional to the electron density N_e), the total line intensity is proportional to N_e^α where $\alpha \in (1, 2)$. Previous model calculations found that the intensity of Fe XIII 1074.7 nm follows a height dependence very close to α=1, indicating that photo-excitation dominates (*48*). We therefore interpreted the derived density at each pixel as the average density inside and outside flux tubes within that pixel. Under such coronal and instrumental conditions, Equation S1 simplifies further to Equation 1. Although Equation 1 is similar in form to the Alfvén speed equation, it describes the properties of kink waves observed by UCoMP. In extreme cases where the derived density is predominantly influenced by higher-density regions (e.g., inside coronal loops) due to higher contributions from collisional excitation, the density contrast between the interior and exterior of the loops could impact the derived magnetic field strengths (*49*). Typical density contrasts of quiescent coronal loops are ~3 to 10 (*50*), so even in the extreme case of the derived density representing the density within coronal loops, the resulting magnetic field strength is biased by $\lesssim$ 30%. Previous forward modeling studies of propagating kink waves have demonstrated that Equation 1 has errors <20% for density contrasts of 2 to 15 (*27*).

1.2.2 Density diagnostics

We used the intensity ratio between the Fe XIII 1074.7 nm and 1079.8 nm lines as a diagnostic of the electron density in the solar corona (*51, 52*). We used the atomic data from CHIANTI to calculate the theoretical relationship between the line ratio and electron density, and combined this relationship with the observed line ratio to diagnose the electron density at each pixel within the FOV of UCoMP. For further details regarding our method, we refer to the previous publications (*21, 22*).

1.2.3 Wave tracking

We modified a wave tracking technique developed in previous work (*17, 21, 22, 26*) to enhance the speed and accuracy of computations.

The wave tracking technique comprises two main steps: the calculation of wave propagation

direction and the calculation of wave phase speed. To determine the wave propagation direction, we first obtained a filtered Doppler velocity time series with a regular cadence of ~33.5 s. The power spectrum of the Doppler velocity of these wave observations has a peak frequency of approximately 3.5 mHz, corresponding to a period of around 5 minutes (*18, 53*). Our sampling cadence is 33.5 s, meaning that we have approximately 9 samples within each wave period, sufficient to determine the wave properties. For each pixel within the FOV, we selected a box of 41×41 pixels centered around the pixel. Using cross correlation, we calculated the coherence between the Doppler velocity time series at the target pixel and those at its surrounding pixels. Regions with high coherence have elongated shapes. To calculate the propagation direction, a linear function was fitted to the elongated region. We modified this calculation to use weighted linear fitting, with higher weights assigned to pixels with higher coherence values, because the propagation of transverse waves favors regions with higher coherence. By repeating this process for each pixel in the observed FOV, we obtained a map of wave propagation direction. Fig. 1, C, F and I provide three examples of coronal wave propagation direction maps.

From the wave propagation direction maps, the wave path was derived for each pixel within the FOV. We then constructed a Doppler velocity time-distance diagram for each wave path. We modified this step to address potential issues with averaging and smoothing the time series that could bias the results. In the previous method, a high-S/N velocity time series was first derived as the reference time series from the time-distance diagram by cross-correlating and averaging the time series along the wave path (*17, 26*). However, this averaging process sometimes introduces smoothing artifacts that bias the results. We therefore modified the method by selecting only the time series from the center pixel of the wave path as our reference time series. By cross-correlating the reference times series (the central time series) with other time series along the wave path, we obtained the time lag (number of pixels required to slide one time series over the other to achieve maximum correlation) and the corresponding correlation coefficient after sliding the time series. Weighted linear fitting was applied to the relative position along the wave path versus the time lag. Higher weights were assigned to points with higher correlation coefficients obtained during the cross-correlation analysis. The phase speed at each pixel was then calculated using the weighted linear fits.

Wave reflection and nonlinearity could also impact the wave tracking results. Waves in the corona can undergo reflection during propagation. Transverse waves observed in the corona using CoMP sometimes experienced reflection, resulting in inward and outward propagating components (*26*). We followed previous work (*21, 22, 26*) by isolating the outward propagating component for the calculation of wave propagation direction and phase speed. Compared to the downward propagating component, this component typically exhibits a higher wave power and, consequently, a higher S/N, making it more suitable for wave tracking analysis.

Previous studies have shown that nonlinearity could enhance wave damping (*54, 55*), resulting in reduced wave amplitudes. The calculation of wave phase speed relies on cross-correlation of the Doppler velocity time series, which requires identification of periodic variation in wave amplitude. If the wave amplitude becomes too small to resolve its periodic variation, the accuracy of cross-correlation (as well as the calculation of phase speed) will be compromised. We investigated our observations for signs of wave damping but did not find any, so assumed that its impact is

negligible. Previous studies using CoMP observations also found weak damping for propagating kink waves (*56*).

The wave tracking results could also be impacted by loop structures (e.g., loop curvature) and magnetic field nonuniformity (e.g., multi-stranded loops and multiple loops within a pixel) (*27, 57-59*). Previous work (*60, 61*) has found that the loop curvature has a very weak impact on the kink oscillations, so the dispersion relation we derived based on a straight cylindrical flux tube is barely affected. Multi-stranded loops with non-twisting threads often show collective behavior and share the same oscillation pattern (*58, 62*), so our results will not be affected. Previous forward modeling has also demonstrated that multi-stranded loops have minimal impact on the validity of Equation 1 in deriving the magnetic field strength (*27*). In the presence of separate loops with different oscillation properties, the interaction between loops has minimal impact on the wave properties if the loops are well-separated (*63, 64*). However, in regions where different loops are in close proximity in distance (within approximately the loop diameter), the derived wave parameters could be affected (*63, 64*), which would lead to higher uncertainty in our measurements.

1.2.4 Estimation of uncertainties

Equation 1 shows that the uncertainty in the magnetic field strength can be obtained by propagating the uncertainties in the phase speed and the density.

During the wave tracking process, the phase speed was determined through weighted linear fitting. Therefore, we determined the uncertainty in the phase speed using the uncertainty in the fitted slope (*21*).

Previous work (*21, 22*) has shown that the uncertainty in density is associated with the uncertainties of the measured line intensities and the inherent systematic uncertainty in the theoretical density-line ratio relationship. Following those studies, we calculated the uncertainty introduced by the theoretical relationship. The UCoMP measurement uncertainty was determined using the same approach in previous work (*21, 22*). To convert the uncertainty in ppm to photon counts, a conversion factor k was used. UCoMP has a different k to CoMP, which was determined using the values of parameters "FLATDN" and "BOPAL" from the headers of the level-1 .fits files ($k = \frac{\mathrm{FLATDN}}{\mathrm{BOPAL}} * 4.12$).

Fig. S2 shows the estimated uncertainties for the inferred coronal magnetic field strengths shown in Fig. 1. The uncertainty is <20% at most locations.

As discussed in Sect. 1.2.3, the magnetic field direction (wave propagation angle) was determined by using linear fitting that minimizes the perpendicular distances of the data points in the high-coherence region from the line being fitted (*26, 65*). The parameter to be minimized, $R_{\perp 0}^2$, is

$$R_{\perp 0}^2 = \sum_{i=1}^{N} \frac{(Y_i - KX_i)^2}{1+K^2} \quad \text{(S2)}$$

where X_i and Y_i are the coordinates of each data point in the high-coherence region, K is the slope of the fitted line, N is the total number of data points, and i is the index of data points. To estimate the uncertainty associated with the fitted angle, a small perturbation of $\Delta\alpha = 2^\circ$ was applied to the best-fitted angle α_0 (related to the slope of the best-fitted line, K_0), resulting in

$\alpha_- = \alpha_0 - \Delta\alpha$ and $\alpha_+ = \alpha_0 + \Delta\alpha$. The angles α_- and α_+ correspond to slopes K_- and K_+, respectively. The to-be-minimized parameter, $R_\perp^2$, increases as the line slope K deviates from K_0 towards K_- and K_+:

$$R_{\perp,-}^2 = \sum_{i=1}^{N} \frac{(Y_i - KX_i)^2}{1+K_-^2} \text{ and } R_{\perp,+}^2 = \sum_{i=1}^{N} \frac{(Y_i - KX_i)^2}{1+K_+^2} \quad \text{(S3)}$$

If the data points are more closely aligned with the fitted line, any deviation in the slope causes the data points to move away from the deviated line. Therefore, even a slight change in the slope can result in a large variation in $R_\perp^2$, indicating that the fitted slope is more precisely determined (the uncertainty in the fitted slope is small). Conversely, when the data points are more scattered, a small change in the fitted slope causes only a small variation in $R_\perp^2$. This indicates that the linear fit is poorly constrained, resulting in a larger uncertainty in the fitted slope. The uncertainty in the fitted angle σ_α was estimated to be inversely related to the variation in $R_\perp^2$ in the presence of a small perturbation of the fitted angle:

$$\sigma_\alpha = \frac{\Delta\alpha}{\sqrt{(R_{\perp,-}^2 - R_{\perp 0}^2) + (R_{\perp,+}^2 - R_{\perp 0}^2)}} \quad \text{(S4)}$$

This equation reflects the uncertainty in the angle calculation due to the scatter of data points and the fitting process.

Fig. S3 shows the estimated uncertainties for the inferred coronal magnetic field directions (wave propagation angles) shown in Fig. 1. We found that the uncertainties are generally <2 degrees at most locations. However, in higher coronal regions with a low S/N, the uncertainties are larger.

1.2.5 Construction of the coronal Carrington maps

From the UCoMP observations, we derived 114 maps of global coronal magnetic field. Each map consists of the east limb and west limb, which correspond to different Carrington longitudes. Assuming minimal coronal structure evolution during one solar rotation, the measuremens from west and east limbs represent coronal magnetic fields approximately 1/4 Carrington rotation before and after the time of observation, respectively.

For each limb measurement on each map, we calculated the latitudinal distribution of coronal magnetic field strength averaged over a distance of 0.01 solar radius. This range extends from 1.05 solar radii to the outermost height, which varies between datasets. The spatial size of the angular resolution element changes with height (solar radii), which we took into account during the averaging. By associating each map with its central meridian and corresponding Carrington rotation number, we calculated the Carrington longitudes of the two latitudinal distribution stripes. The 114 maps yielded 228 stripes of latitudinal distributions corresponding to different Carrington longitudes across various Carrington rotations.

To construct the synoptic Carrington maps, we interpolated the latitudinal distribution stripes along the Carrington longitude direction, to obtain a Carrington map with its Y-axis representing latitude and its X-axis representing Carrington longitude. We derived Carrington maps of coronal magnetic field strength, intensity and density across various coronal heights. Although the HMI synoptic photospheric magnetograms have been corrected for solar B-angle (the angle between the solar equatorial plane and the ecliptic plane), the latitude in our coronal Carrington maps was not corrected for B-angle. This is because the off-limb measurements are LOS integrated,

complicating any correction for B-angles. Our data span B-angles between only -7.23 and +7.23 degrees, so we assumed that the effect is negligible.

For the Carrington maps of photospheric magnetic field, we used the synoptic maps from HMI measurements during CR2254 to CR2263. To match the angular resolution of the coronal Carrington maps, we degraded the angular resolution of the photospheric Carrington maps as follows: i) Converted the Y-axis of the original HMI photospheric Carrington map from sine latitude to colatitude (90° minus latitude), then interpolated the Y-axis to uniform colatitudes θ_{co}; ii) Took the absolute value of the radial component of the magnetic field $|B_{\mathrm{r}}|$, and multiplied by $\sin\theta_{\mathrm{co}}$ to ensure that flux is preserved during degrading; iii) Degraded the Carrington map to the desired angular resolution by dividing the map into small regions and averaging values inside each small region.

Fig. 2 shows examples of Carrington maps of photospheric magnetic field measured by HMI, coronal magnetic field strength, line emission intensity and electron density averaged between 1.10 and 1.15 solar radii, and between 1.20 and 1.25 solar radii, derived from the UCoMP observations. These Carrington maps cover five Carrington rotations from CR2258 to CR2262. We found that regions with higher density generally exhibit higher coronal magnetic field strengths, which is expected since stronger-field regions such as active regions generally have higher densities.

Fig. 3 shows snapshots from the spherical distributions of magnetic field at different heights, obtained by reprojecting the Carrington maps from each Carrington rotation onto a spherical coordinate system.

1.2.6 Calculation of LOS emissivity-weighted parameters

To facilitate comparison between the models and observations, investigate any discrepancies between them, and determine the potential effects of LOS integration, we calculated the LOS emissivity-weighted coronal parameters from the MAS models. These LOS weighted parameters were determined using Equation 2. For each pixel within the UCoMP FOV, we computed the LOS distributions of coronal emissivity, B_{y} (the coronal magnetic field component along X-direction on the POS) and B_{z} (the coronal magnetic field component along Y-direction on the POS) from one solar radius behind to one solar radius in front of the POS crossing the solar center with an interval of 0.01 solar radius. We followed conventional notations B_{y} and B_{z} to describe the two magnetic field components in the models.

The POS component of coronal magnetic field strength is $B_{\mathrm{POS}} = \sqrt{B_{\mathrm{y}}^2 + B_{\mathrm{z}}^2}$. We calculated the LOS emissivity-weighted coronal magnetic field strength (POS component) $\overline{B_{\mathrm{POS}}}$ for each pixel within the FOV as:

$$\overline{B_{\mathrm{POS}}} = \frac{\int_{-1R_{\mathrm{S}}}^{+1R_{\mathrm{S}}} B_{\mathrm{POS},i} \cdot \varepsilon_i \, \mathrm{d}l}{\int_{-1R_{\mathrm{S}}}^{+1R_{\mathrm{S}}} \varepsilon_i \, \mathrm{d}l} \qquad \text{(S5)}$$

where $B_{\mathrm{POS},i}$ and ε_i are the POS component of coronal magnetic field strength and emissivity of Fe XIII 1074.7 nm at location *i* along the LOS, respectively. The integrals were taken along the

LOS from -1R_s to +1R_s, because the emissivity drops quickly when it approaches larger heights above the solar surface. We do not perform weighted averaging of magnetic field vectors, but of B_{POS}. This is partially connected to the wave observations and the technique of coronal seismology. The magnetic field strength measured using UCoMP wave observations is based on the wave phase speed, which is a scalar quantity that is only dependent on the strength of the magnetic field and not its direction.

Similarly, we computed the LOS emissivity-weighted coronal magnetic field direction (POS component) $\overline{\Psi_{\mathrm{POS}}}$. Because the waves propagate along field lines, the measured wave propagation directions provide information about the field directions. The wave propagation directions are solely determined by the field directions. Therefore, we calculated the emissivity-weighted directions without involving magnetic field vectors. Firstly, for each location *i* along each LOS, we calculated the coronal magnetic field direction (POS component) as

$$\Psi_{\mathrm{POS}} = \tan^{-1}\left(\frac{B_z}{B_y}\right) \qquad \text{(S6)}$$

The resulting value of Ψ_{POS} was then converted to $\Psi_{\mathrm{POS}}^{\mathrm{rad}}$, the direction with respect to the local radial direction. $\Psi_{\mathrm{POS}}^{\mathrm{rad}}$ is defined as positive if it is counterclockwise from the local radial direction, and negative otherwise. We limit its range to $(-90^{\circ}, 90^{\circ})$, due to the 180°-ambiguity. The LOS emissivity-weighted coronal magnetic field direction (POS component) $\overline{\Psi_{\mathrm{POS}}}$ for each pixel within the FOV was calculated as:

$$\overline{\Psi_{\mathrm{POS}}} = \frac{\int_{-1R_s}^{+1R_s} \Psi_{\mathrm{POS},i}^{\mathrm{rad}} \cdot \varepsilon_i \, \mathrm{d}l}{\int_{-1R_s}^{+1R_s} \varepsilon_i \, \mathrm{d}l} \qquad \text{(S7)}$$

where $\Psi_{\mathrm{POS},i}^{\mathrm{rad}}$ and ε_i are the POS component of coronal magnetic field direction (with respect to local radial direction) and emissivity of Fe XIII 1074.7 nm at location *i* along the LOS, respectively. The integrals were taken along the LOS from -1R_s to +1R_s.

2. Supplementary Text

2.1 Evolution of coronal magnetic field

Previous photospheric observations have shown a phenomenon referred to as activity nests, in which newly-emerging active regions tend to appear at similar locations as the previous active regions or in close proximity to existing ones (*31, 32*). This behavior is closely associated with the recurrent emergence of magnetic flux at certain longitudinal sectors from beneath the photosphere, known as active longitudes. From photospheric observations of the Sun's front side by SDO/HMI and helioseismic estimations of the far-side photospheric magnetic features (*66-68*; here we used data from June 2022 to August 2022), we found that active regions in our eight-month observational period typically did not survive a full solar rotation; instead, new active regions often emerged in the vicinity of previously existing active regions. For example, the active regions designated AR13030, AR13031 and AR13032 disappeared within one solar rotation, while new active regions AR13053 and AR13055 emerged near the previously dissipated active regions. From our Carrington maps of the coronal magnetic field, we found a recurrent pattern of strong-field features at similar longitudes in the corona (Fig. 2, B and E), which corresponds to the repeated emergence of different active regions in similar longitudinal sectors during different

Carrington rotations. This indicates that active longitudes extend their influence to the coronal magnetic field.

The coronal magnetic field strengths of active regions in the Carrington maps also exhibit fluctuations over several solar rotations. For example, the maximum values of the magnetic field strength between 1.10 and 1.15 solar radii varies from ~10 G to ~20 G in the corona above different active regions during our eight-month observational period. In contrast, the maximum magnetic field strengths in most other regions within this height range are <5 G.

2.2 Comparison with MAS models

Coronal observations using optically thin spectral lines are subject to the LOS integration effect. Our analysis assumed that the observed quantities represent the emissivity-weighted results along the LOS. To verify this assumption and investigate the impact of LOS integration on the measured physical quantities, we compared our measurements with predictions from the MAS models.

We calculated the LOS emissivity-weighted coronal magnetic field strength and direction (POS component) from the MAS models as described in Section 1.2.6. Figure 5 compares the coronal magnetic field from the UCoMP observations with the LOS emissivity-weighted quantities from the MAS models. Fig. 5A-B shows that the observational measurements and model predictions are correlated. For Fig. 5A, the Pearson correlation coefficient is 0.64. This supports our assumptions that the measured coronal magnetic field strength corresponds to the LOS emissivity-weighted values, and that the wave propagation direction used to infer the field direction from the observation reflects the coronal magnetic field direction.

Despite the general correlation, we also found discrepancies between the observational measurements and the model predictions. In Fig. 5A the magnetic field strengths in active regions (identifiable as those with stronger observed field) are under-predicted by the models. We attribute this discrepancy to two effects: i) The synoptic photospheric magnetic field maps used as input to the MAS models do not include any time variation or 3D vector field information, and the need for 27 days of data means that they do not include any newly developed active regions or other magnetic structures near the solar limbs. ii) Active regions contain more complex magnetic and thermodynamic structures than quiet-Sun regions, so the LOS integration effect is also more complex and modelling the complicated plasma structures in these regions is more challenging. The MAS models we used have low spatial resolution and adopted empirical heating terms. This could partly explain the absence of fine structures in the model predictions. We noticed that higher-resolution simulations have produced filamentary structures of the magnetic field in LOS emissivity-weighted model predictions (*14*).

We found even larger discrepancies in the magnetic field strength for regions at higher latitudes. Fig. 5C shows the relationship between B_{MAS} and B_{obs} for regions with latitudes exceeding 50° in both the northern and southern hemispheres. There is a much larger discrepancy than at lower latitudes: the Pearson correlation coefficient is only 0.34. We attribute the lower correlation in high-latitude regions to the less reliable measurements of the high-latitude photospheric magnetic field, due to projection effects and unobserved polar regions (*69*). There is no trend in Fig. 5C in the discrepancy as a function of coronal magnetic field strength. However, in some regions with

lower intensity, large discrepancies appear in the field directions. We attribute this to the higher uncertainty in field direction in such regions due to the lower S/N (Fig. S3).

Some of the discrepancies between observations and model results could instead arise from the calculation of the LOS emissivity-weighted parameters. Although that calculation is a linear operation, the derivations of the phase speed, density, magnetic field strength and direction are all non-linear operations. Therefore, the linear averages of the field strength and direction from the models are only first-order approximations, which could deviate from the observed parameters. Nevertheless, we found that the LOS emissivity-weighted parameters predicted by the models are sufficient for comparison purposes.

We conclude that the observationally measured coronal magnetic fields are generally consistent with the predictions of the models (maps of LOS emissivity-weighted field). We do not expect a perfect correspondence due to the limitations of LOS emissivity-weighting, the absence of real-time information and polar observations in the boundary photospheric magnetograms.

2.3 Comparison between observations and PFSS models

We also compared the observations to simpler coronal magnetic field extrapolation models using the potential-field source surface (PFSS) method.

The wave phase speeds we measured from the observations are the projection of the true speeds onto the POS, so the measured field strengths should correspond to the POS projection of the coronal magnetic field (*21, 22*). Due to the LOS integration effect, for each pixel within the FOV the measured magnetic field (both strength and direction) represents the emissivity-weighted average of the POS projection of the magnetic field vector at each grid point along the LOS. Because PFSS models lack information about the plasma temperature and density, we cannot use them to calculate emissivity or emissivity-weighted parameters. We compared the UCoMP measurements with the POS component of the magnetic field on the plane crossing the solar center and perpendicular to the LOS predicted by the PFSS models described in section 1.1.5 above.

Figure S4A-B shows the maps of coronal magnetic field strength from the UCoMP observations on 21 February 2022 and the corresponding PFSS model. To compare the height distributions of the magnetic field, we selected four annulus sectors (corresponding to two active regions and two quiet-Sun regions, labelled in Fig. S4A-B) and plotted the variation of average field strength as a function of radial distance within each sector (Fig. S4C-F).

We found some large-scale similarities between observational measurements of UCoMP and the predictions from the PFSS model. For example, both maps show higher coronal magnetic field strengths above active regions. However, we also identified many discrepancies. For example, the PFSS model predicts high field strengths in polar regions, which could be due to the unreliable magnetic field information of these regions in the boundary photospheric magnetograms. The average coronal magnetic field strengths from the observations and models follow similar decreasing trends with height, but differ in magnitude. As discussed in previous work (*21*), such discrepancies could arise from the violation of the potential-field assumption (made by the PFSS

models) in certain regions, particularly above active regions where the coronal magnetic field is unlikely to be potential field. We also used a different definition of B_{POS} between the observational measurement and the PFSS model prediction. For the observational measurement, the magnetic field was determined as the emissivity-weighted average of the POS projection of the magnetic field vector at each grid point along the LOS, whereas the PFSS model provides only the magnetic field on a single POS. This difference should also contribute to the discrepancies between the two results. In addition, the various factors that can potentially impact the accuracy of our method, as discussed in Sect. 1.2.3, may also contribute to the discrepancies found here. The comparisons with both MAS models and PFSS models suggest that coronal MHD models align more closely with observational data, and are more suitable for an investigation of the impact of LOS integration effect on coronal observations.

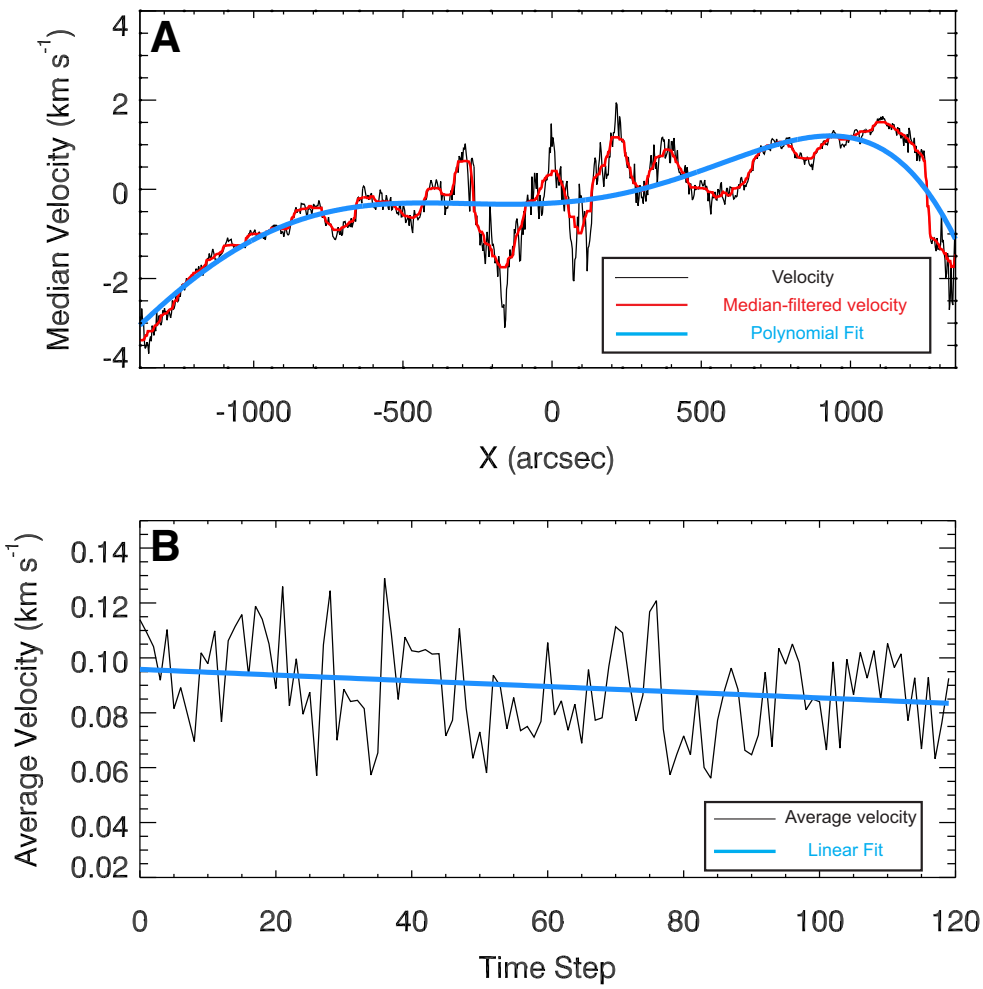

Fig. S1. Examples of Doppler velocity trend corrections. (A) The correction for the east-west Doppler velocity trend. This example uses the Doppler velocity image obtained on 19:54:54 UT on 24 February 2022. For every position along X direction (east-west direction), the median value of the Doppler velocity along Y direction (north-south direction) was calculated. The black curve shows the median velocity variation along the east-west direction. The red curve is the median-filtered (in a window of 21 pixels) result of the black curve, with the purpose of removing possible abnormal values. A 5th order polynomial fit was applied to the red curve (shown as the blue curve). This polynomial function describes the east-west variation of the Doppler velocity and will be subtracted from the original Doppler velocity image. **(B)** The correction for the temporal trend of Doppler velocity throughout continuous observation each day. This example shows the correction for the Doppler velocity time series obtained from 19:54:54 UT to 21:01:33 UT on 24 February 2022. For each time step, the average Doppler velocity within the FOV was calculated (black curve). A linear fitting was applied to the time series of the average Doppler velocity to show

potential temporal trend (blue curve), which will be subtracted from the Doppler velocity time series.

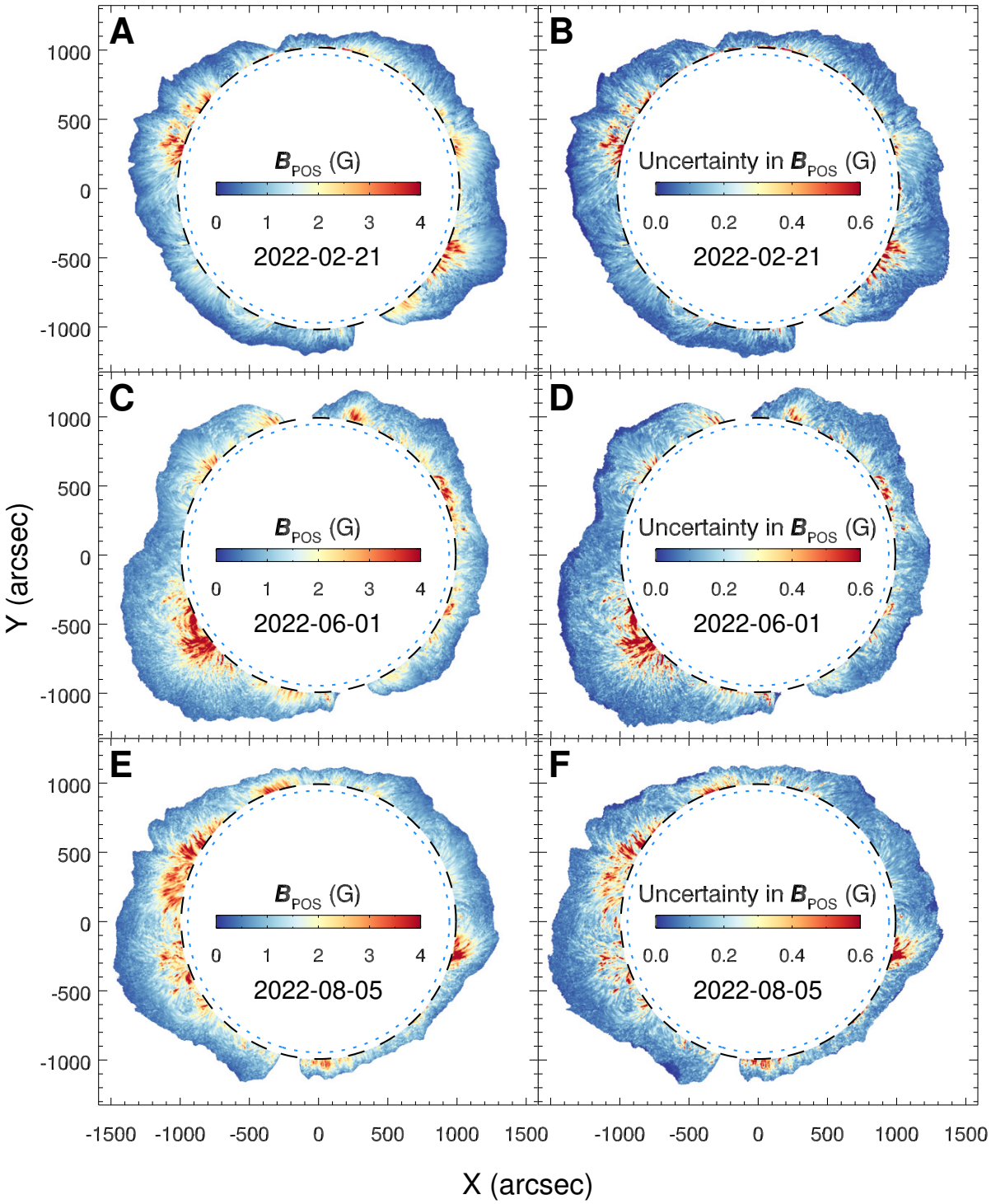

Fig. S2. Uncertainty on the measured coronal magnetic field strength. (**A, C, E**) Same as Figure 1B, E, H. (**B**, **D**, **F**) The corresponding uncertainties for each of the three measurements, on a different color scale.

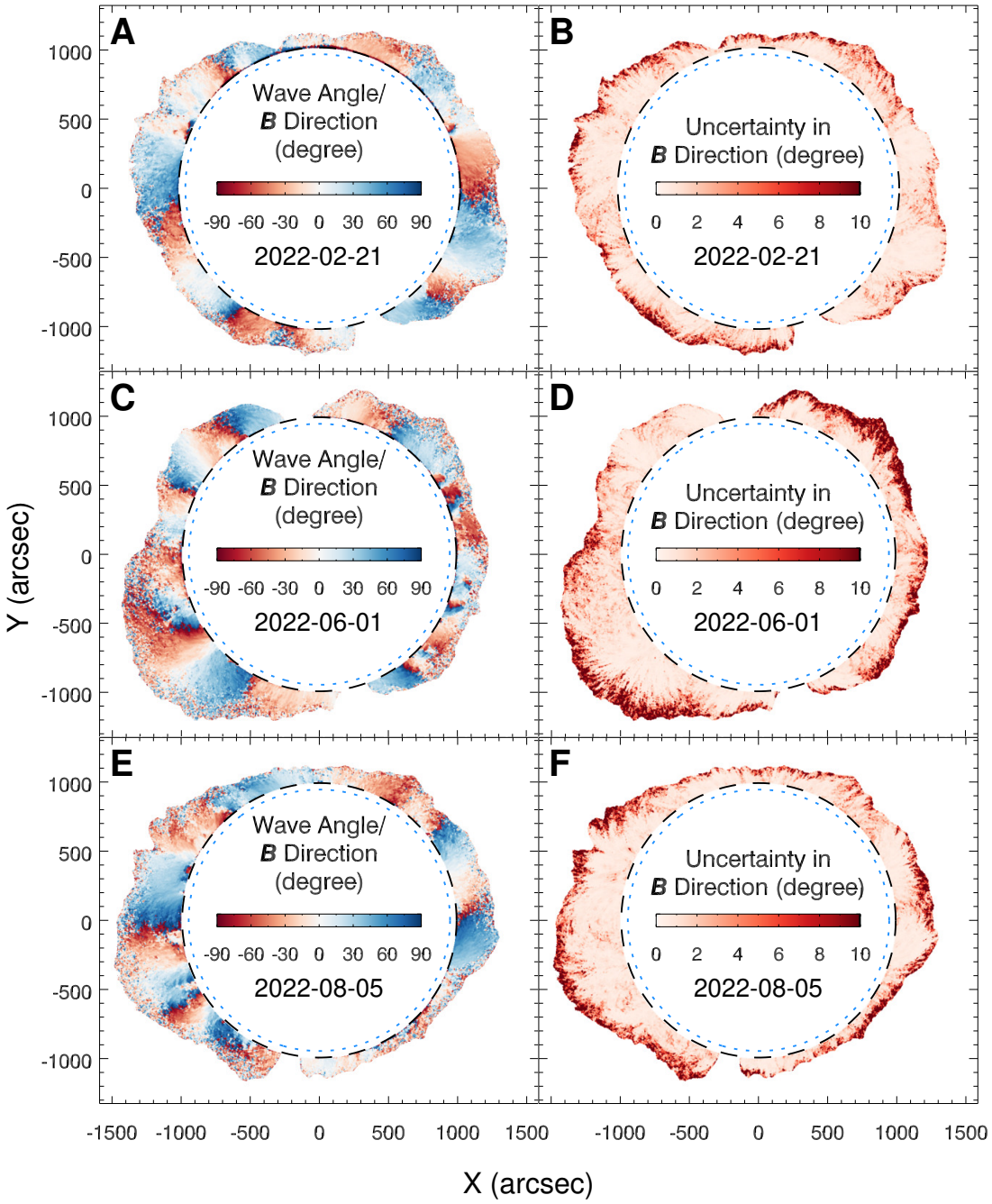

Fig. S3. Uncertainty on the inferred coronal magnetic field direction. These uncertainties were determined from the wave propagation angle. (**A, C, E**) Same as Figure 1C, F, I. (**B**, **D**, **F**) The corresponding uncertainties for each of the three measurements, on a different color scale.

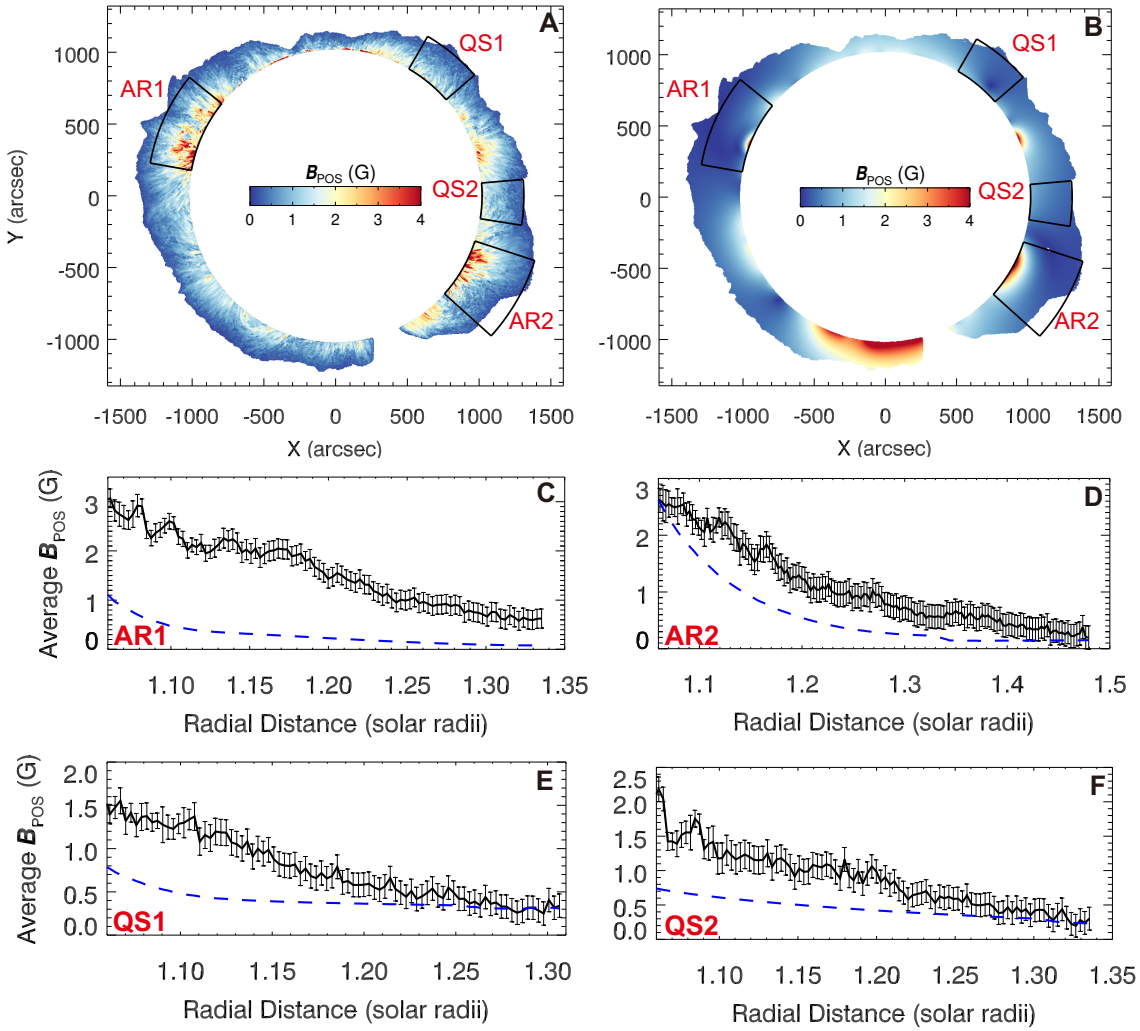

Fig. S4. Comparison between the UCoMP measurements and PFSS model predictions. The data are for the UCoMP observations on 21 February 2022 and predictions from a PFSS model using the corresponding HMI synoptic magnetogram as input. **(A)** The same magnetic field strength map as Fig. 1B, but with four annulus sectors overlain marking two active regions (AR1, AR2) and two quiet-Sun regions (QS1, QS2). **(B)** The magnetic field strength on the POS that crosses the solar center predicted by the PFSS model. **(C)-(F)** The average magnetic field strengths as a function of radial distance within the annulus sectors from the UCoMP measurement (black solid line) and PFSS model (blue dashed line). Error bars indicate the standard errors on the mean values in each radius bin.

Table S1. Log of the UCoMP observations. We used 114 UCoMP datasets, each consisting of several frames of Fe XIII 1074.7 nm and 1079.8 nm intensity images for plasma density diagnostics, followed by a continuous image sequence used for wave tracking. N indicates the number of frames used for analysis.

UT Date	Wave tracking		Fe XIII 1074.7 nm		Fe XIII 1079.8 nm	
	UT range	N	UT range	N	UT range	N
2022-02-19	19:47:04-20:53:42	120	18:51:15-19:21:39	4	18:56:34-19:26:57	4
2022-02-20	19:51:10-20:57:47	120	18:55:17-19:25:36	4	18:00:44-19:31:03	4
2022-02-21	19:47:45-20:54:21	120	18:51:50-19:22:20	4	18:57:08-19:27:37	4
2022-02-23	19:47:30-20:58:43	120	18:51:45-19:22:04	4	18:57:02-19:27:22	4
2022-02-24	19:54:54-21:01:33	120	19:26:45-19:29:17	2	19:32:13-19:34:45	2
2022-02-26	19:44:24-20:51:03	120	18:48:46-19:18:58	4	18:54:04-19:24:16	4
2022-02-28	19:43:53-20:50:35	120	18:42:31-19:18:27	4	18:53:34-19:23:45	4
2022-03-01	19:29:55-20:35:18	115	18:29:45-18:59:57	4	18:35:03-19:05:15	4
2022-03-03	19:46:02-20:53:12	120	18:41:21-19:20:22	4	18:46:41-19:25:44	4
2022-03-05	23:33:42-00:40:19 (+1 day)	120	22:34:40-23:07:28	4	22:40:05-23:12:54	4
2022-03-06	19:36:13-20:42:47	120	18:40:21-19:10:51	4	18:45:49-19:16:08	4
2022-03-07	19:26:57-20:46:53	120	18:31:24-19:01:36	4	18:36:41-19:06:54	4
2022-03-09	19:37:33-20:31:17	97	18:41:41-19:12:11	4	18:46:59-19:17:29	4
2022-03-12	19:13:20-20:19:56	120	18:17:37-18:47:58	4	18:22:54-18:53:16	4
2022-03-13	19:40:07-20:46:41	120	18:44:16-19:14:46	4	18:52:06-19:20:03	3
2022-03-19	20:32:58-21:39:36	120	19:37:05-20:07:26	4	19:42:22-20:12:53	4
2022-03-20	19:08:35-20:15:15	120	18:11:40-18:43:11	4	18:16:58-18:48:29	4
2022-03-21	02:58:27-04:05:04	120	02:02:35-02:33:05	4	02:07:52-02:38:23	4
2022-03-21	19:24:18-20:37:07	120	18:28:33-18:58:56	4	18:33:51-19:04:14	4
2022-03-24	19:06:26-20:13:18	120	17:56:38-18:55:04	4	18:02:16-19:00:32	4
2022-03-25	20:46:08-21:53:05	120	19:50:10-20:20:39	4	19:55:28-20:25:58	4
2022-03-27	19:36:40-20:44:13	120	18:40:47-19:10:58	4	18:46:05-19:16:25	4
2022-03-31	19:16:58-20:23:33	120	18:21:14-18:51:25	4	18:26:31-18:56:43	4
2022-04-01	19:26:23-20:33:01	120	18:30:16-19:00:38	4	18:35:34-19:06:06	4
2022-04-03	20:37:41-21:37:02	106	19:42:10-20:12:20	4	19:47:27-20:17:38	4
2022-04-10	18:54:44-19:25:33	56	17:58:49-18:29:11	4	18:04:07-18:34:29	4
2022-04-13	19:20:37-20:27:16	120	18:24:52-18:55:14	4	18:30:10-19:00:32	4
2022-04-24	20:37:28-21:43:28	120	19:28:49-20:12:50	4	19:34:04-20:18:05	4
2022-04-26	00:21:52-01:27:50	120	23:26:45 (-1 day) - 23:56:41 (-1 day)	4	23:32:00 (-1 day) - 00:01:56	4
2022-04-27	20:34:30-21:40:33	120	19:35:07-19:37:39	2	20:12:03-20:14:34	2
2022-05-13	19:26:04-20:32:06	120	18:30:41-19:00:51	4	18:35:57-19:06:07	4
2022-05-14	19:53:27-20:54:20	108	18:50:09-19:20:08	4	18:55:24-19:25:23	4
2022-05-21	19:56:10-21:02:13	120	19:00:50-19:30:59	4	19:06:06-19:36:14	4
2022-05-22	19:41:39-20:47:42	120	18:45:01-19:16:15	4	18:51:21-19:21:40	4
2022-05-23	18:56:36-20:02:38	120	18:00:09-18:30:16	4	18:05:24-18:36:31	4
2022-06-01	18:34:06-19:40:09	120	17:38:45-18:08:54	4	17:44:00-18:14:10	4
2022-06-02	19:07:57-20:13:58	120	18:12:47-18:42:45	4	18:18:02-18:48:01	4
2022-06-04	18:38:21-19:44:22	120	17:43:03-18:13:00	4	17:48:18-18:18:26	4
2022-06-06	19:04:29-20:10:30	120	18:09:17-18:39:16	4	18:14:32-18:44:31	4
2022-06-07	18:36:50-19:42:52	120	17:41:29-18:11:28	4	17:46:44-18:16:44	4

2022-06-08	18:36:40-19:42:42	120	17:41:20-18:11:29	4	17:46:35-18:16:44	4
2022-06-09	18:42:12-19:48:14	120	17:47:01-18:17:00	4	17:52:16-18:22:16	4
2022-06-10	21:01:40-22:07:42	120	20:33:57-20:36:28	2	20:39:12-20:41:44	2
2022-06-11	18:44:54-19:50:55	120	17:49:35-18:19:43	4	17:55:00-18:24:58	4
2022-06-13	00:58:34-02:04:36	120	00:03:05-00:33:14	4	00:10:51-00:38:29	3
2022-06-13	19:38:19-20:44:23	120	18:43:00-19:13:07	4	18:48:15-19:18:23	4
2022-06-14	18:41:56-19:47:58	120	17:46:20-18:16:30	4	17:51:35-18:21:55	4
2022-06-16	18:52:50-19:58:54	120	17:56:07-18:26:11	4	18:01:25-18:31:27	4
2022-06-19	18:51:46-19:57:50	120	17:56:00-18:26:10	4	18:01:16-18:31:45	4
2022-06-20	18:42:40-19:48:43	120	17:47:27-18:17:26	4	17:52:42-18:22:41	4
2022-06-21	18:46:14-19:52:15	120	17:51:00-18:21:01	4	17:56:16-18:26:16	4
2022-06-24	18:59:58-20:06:00	120	18:04:45-18:34:45	4	19:10:01-18:40:01	4
2022-06-25	18:42:45-19:39:54	104	17:47:22-18:17:32	4	17:52:38-18:22:48	4
2022-06-27	22:13:12-23:18:40	119	21:45:28-21:48:00	2	21:50:44-21:53:15	2
2022-07-03	19:36:02-20:16:34	74	18:39:20-10:09:20	4	18:44:35-19:16:06	3
2022-07-04	20:40:35-21:46:37	120	20:12:52-20:15:53	2	20:18:07-20:20:39	2
2022-07-05	21:07:33-22:13:36	120	20:08:06-20:42:22	4	20:13:21-20:47:37	4
2022-07-07	19:26:07-20:18:50	95	18:30:56-19:00:56	4	18:36:12-19:06:12	4
2022-07-09	18:49:19-19:55:21	120	17:53:42-18:23:42	4	17:58:59-18:29:07	4
2022-07-10	19:27:07-20:33:09	120	18:31:46-19:01:56	4	18:37:01-19:07:11	4
2022-07-12	18:52:14-19:58:17	120	17:56:45-18:26:53	4	18:02:10-18:32:08	4
2022-07-14	19:08:52-20:14:53	120	18:13:11-18:43:39	4	18:18:26-18:48:56	4
2022-07-17	20:00:16-21:06:18	120	19:04:36-19:34:55	4	19:09:53-19:40:20	4
2022-07-18	18:55:31-19:28:49	61	17:49:24-18:19:31	4	17:54:39-18:24:57	4
2022-07-20	19:18:31-20:24:34	120	18:23:09-18:53:19	4	18:28:25-18:58:34	4
2022-07-21	19:25:28-20:31:31	120	18:20:52-18:57:06	4	18:26:17-19:02:22	4
2022-07-22	19:16:48-20:23:28	120	18:11:53-18:48:13	4	18:17:11-18:53:31	3
2022-07-24	19:08:21-20:14:59	120	18:03:26-18:39:47	4	18:08:44-18:45:05	4
2022-07-25	19:35:08-20:39:00	115	18:25:54-19:06:30	4	18:31:13-19:11:48	4
2022-07-26	19:31:42-20:38:19	120	18:26:27-19:02:58	4	18:31:45-19:08:16	4
2022-07-27	19:21:03-20:27:41	120	18:09:36-18:50:20	4	18:14:54-18:55:38	4
2022-07-28	19:39:23-20:12:59	61	18:27:57-19:08:42	4	18:33:15-19:14:00	4
2022-07-30	21:42:45-22:18:02	64	20:31:06-21:11:51	4	20:36:24-21:17:18	4
2022-07-31	19:30:17-20:33:35	114	18:18:50-18:59:35	4	18:24:08-19:04:53	4
2022-08-01	19:50:37-20:41:01	91	18:32:00-19:19:55	4	18:37:18-19:25:13	4
2022-08-02	19:36:30-20:30:49	98	18:24:53-19:05:38	4	18:30:11-19:10:56	4
2022-08-05	19:31:16-20:37:54	120	18:20:00-19:00:36	4	18:25:18-19:05:53	4
2022-08-06	19:29:04-20:21:10	94	18:17:39-18:58:24	4	18:22:47-19:03:42	4
2022-08-14	19:43:55-20:50:34	120	18:30:20-19:11:54	4	18:35:48-19:17:22	4
2022-08-19	19:49:30-20:22:10	59	18:36:23-19:16:58	4	18:41:41-19:22:15	4
2022-08-23	19:49:31-20:56:12	120	18:38:14-19:18:49	4	18:43:32-19:24:07	4
2022-08-24	19:32:36-20:09:38	60	18:21:18-19:01:55	4	18:26:36-19:07:13	4
2022-08-25	20:02:01-21:08:43	120	18:49:49-19:30:25	4	18:55:07-19:35:43	4
2022-08-27	19:32:31-20:17:53	82	18:20:54-19:01:40	4	18:26:12-19:06:58	4
2022-08-28	19:37:35-20:44:15	120	18:26:00-19:06:44	4	18:31:18-19:12:02	4
2022-08-29	20:06:26-20:56:56	89	18:32:15-19:14:49	4	18:37:33-19:20:07	4
2022-08-30	20:07:09-21:08:11	110	18:51:40-19:36:28	4	18:56:58-19:41:46	4
2022-08-31	19:38:08-20:44:47	120	18:26:51-19:07:27	4	18:32:09-19:12:45	4
2022-09-01	20:09:58-21:16:36	120	18:58:24-19:39:08	4	19:03:52-19:44:26	4

2022-09-04	19:35:21-20:42:02	120	18:23:56-18:26:28	2	18:29:14-18:31:46	2
2022-09-05	20:32:29-21:17:18	81	19:37:27-19:39:59	2	19:42:44-19:45:17	2
2022-09-06	20:01:11-20:30:52	54	18:38:37-19:19:10	4	18:43:55-19:24:28	4
2022-09-08	19:48:46-20:55:25	120	19:14:18-19:16:50	2	19:19:35-19:22:08	2
2022-09-09	20:04:32-21:11:19	109	19:30:47-19:33:19	2	19:36:04-19:38:37	2
2022-09-10	21:21:49-22:03:48	76	19:08:11-20:13:07	4	19:13:28-20:18:24	4
2022-09-12	21:33:44-22:28:02	98	19:33:51-19:36:23	2	19:39:09-19:41:41	2
2022-09-14	19:37:06-20:35:55	95	19:03:21-19:05:54	2	19:08:39-19:11:11	2
2022-09-17	20:24:23-21:13:14	88	18:55:06-19:35:49	4	19:00:23-19:41:06	4
2022-09-18	19:42:49-20:46:06	114	18:28:04-19:08:48	4	18:33:21-19:14:06	4
2022-09-19	20:03:00-21:00:42	104	19:16:32-19:19:04	2	19:22:39-19:25:12	2
2022-09-20	19:51:12-20:50:33	107	18:38:38-19:16:38	3	18:41:23-19:21:56	4
2022-09-22	19:58:01-20:53:26	98	17:59:18-18:39:51	4	18:04:35-18:42:37	3
2022-09-27	20:11:15-21:05:35	98	18:54:57-19:35:30	2	19:02:47-19:40:47	3
2022-09-29	20:43:16-21:12:23	53	19:27:29-19:30:01	2	19:32:46-19:35:19	2
2022-10-12	20:39:09-21:28:59	90	19:23:31-20:04:12	4	19:28:48-20:09:30	4
2022-10-15	20:01:16-21:07:57	120	18:49:41-19:30:36	4	18:55:09-19:35:53	4
2022-10-16	19:52:00-20:31:47	60	19:17:30-19:20:03	2	19:22:48-19:25:20	2
2022-10-17	19:59:03-20:34:21	64	18:47:37-19:28:22	4	18:52:55-19:33:40	3
2022-10-18	20:23:11-21:24:48	111	19:03:25-19:44:00	4	19:08:43-19:49:18	4
2022-10-20	20:01:22-20:40:34	71	18:52:30-19:30:42	3	18:55:16-19:36:00	4
2022-10-23	20:10:27-21:01:25	92	19:21:33-19:24:05	2	19:26:51-19:29:23	2
2022-10-25	20:14:53-21:21:32	120	19:06:10-19:44:12	3	19:08:55-19:49:30	4
2022-10-26	19:48:33-20:28:19	72	18:37:08-19:17:53	4	18:42:35-19:23:11	4
2022-10-29	20:34:05-21:14:26	72	18:38:55-18:41:28	2	18:44:13-18:46:46	2

Caption for Movie S1 (.mp4 file).

The 3.5-mHz filtered Doppler velocity images observed on 21 February 2022.

Caption for Movie S2 (.mp4 file).

All 114 global maps of the coronal magnetic field measured from the UCoMP observations. Plotting symbols are the same as Fig. 1B-C. Note that we obtained two coronal magnetograms on 21 March 2022, and also on 13 June 2022 (from the two datasets observed on each day, see Table S1). For these two days we use "(1)" and "(2)" to identify the two magnetograms.

Caption for Movie S3 (.mp4 file).

The spherical distributions of magnetic field strength in different atmospheric layers. An animated version of Figure 3, showing all meridians over five Carrington rotations. Plotting symbols and color scales are the same as in Fig. 3. (**A**) The photospheric magnetic field (radial component) measured by HMI. (**B**) The coronal magnetic field averaged between 1.10 and 1.15 solar radii derived from the UCoMP observations. (**C**) Same as panel B, except averaged between 1.20 and 1.25 solar radii.

References and Notes

1. T. Wiegelmann, J. K. Thalmann, S. K. Solanki, The magnetic field in the solar atmosphere. *Astron. Astrophys. Rev.* **22**, 78 (2014). doi:10.1007/s00159-014-0078-7

2. T. Samanta, H. Tian, V. Yurchyshyn, H. Peter, W. Cao, A. Sterling, R. Erdélyi, K. Ahn, S. Feng, D. Utz, D. Banerjee, Y. Chen, Generation of solar spicules and subsequent atmospheric heating. *Science* **366**, 890–894 (2019). doi:10.1126/science.aaw2796 Medline

3. R. Ishikawa, J. T. Bueno, T. Del Pino Alemán, T. J. Okamoto, D. E. McKenzie, F. Auchère, R. Kano, D. Song, M. Yoshida, L. A. Rachmeler, K. Kobayashi, H. Hara, M. Kubo, N. Narukage, T. Sakao, T. Shimizu, Y. Suematsu, C. Bethge, B. De Pontieu, A. S. Dalda, G. D. Vigil, A. Winebarger, E. A. Ballester, L. Belluzzi, J. Štěpán, A. A. Ramos, M. Carlsson, J. Leenaarts, Mapping solar magnetic fields from the photosphere to the base of the corona. *Sci. Adv.* **7**, eabe8406 (2021). doi:10.1126/sciadv.abe8406 Medline

4. S. K. Solanki, A. Lagg, J. Woch, N. Krupp, M. Collados, Three-dimensional magnetic field topology in a region of solar coronal heating. *Nature* **425**, 692–695 (2003). doi:10.1038/nature02035 Medline

5. P. F. Wyper, S. K. Antiochos, C. R. DeVore, A universal model for solar eruptions. *Nature* **544**, 452–455 (2017). doi:10.1038/nature22050 Medline

6. H. Lin, M. J. Penn, S. Tomczyk, A new precise measurement of the coronal magnetic field strength. *Astrophys. J.* **541**, L83–L86 (2000). doi:10.1086/312900

7. H. Lin, J. R. Kuhn, R. Coulter, Coronal magnetic field measurements. *Astrophys. J.* **613**, L177–L180 (2004). doi:10.1086/425217

8. D. Kuridze, M. Mathioudakis, H. Morgan, R. Oliver, L. Kleint, T. V. Zaqarashvili, A. Reid, J. Koza, M. G. Löfdahl, T. Hillberg, V. Kukhianidze, A. Hanslmeier, Mapping the magnetic field of flare coronal loops. *Astrophys. J.* **874**, 126 (2019). doi:10.3847/1538-4357/ab08e9

9. B. Chen, C. Shen, D. E. Gary, K. K. Reeves, G. D. Fleishman, S. Yu, F. Guo, S. Krucker, J. Lin, G. M. Nita, X. Kong, Measurement of magnetic field and relativistic electrons along a solar flare current sheet. *Nat. Astron.* **4**, 1140–1147 (2020). doi:10.1038/s41550-020-1147-7

10. G. D. Fleishman, D. E. Gary, B. Chen, N. Kuroda, S. Yu, G. M. Nita, Decay of the coronal magnetic field can release sufficient energy to power a solar flare. *Science* **367**, 278–280 (2020). doi:10.1126/science.aax6874 Medline

11. G. D. Fleishman, G. M. Nita, B. Chen, S. Yu, D. E. Gary, Solar flare accelerates nearly all electrons in a large coronal volume. *Nature* **606**, 674–677 (2022). doi:10.1038/s41586-022-04728-8 Medline

12. W. Li, J. Grumer, Y. Yang, T. Brage, K. Yao, C. Chen, T. Watanabe, P. Jönsson, H. Lundstedt, Roger Hutton, Y. Zou, A novel method to determine magnetic fields in low-density plasma facilitated through accidental degeneracy of quantum states in Fe^{9+}. *Astrophys. J.* **807**, 69 (2015). doi:10.1088/0004-637X/807/1/69

13. E. Landi, R. Hutton, T. Brage, W. Li, Hinode/EIS Measurements of Active-region Magnetic Fields. *Astrophys. J.* **904**, 87 (2020). doi:10.3847/1538-4357/abbf54

14. Y. Chen, W. Li, H. Tian, F. Chen, X. Bai, Y. Yang, Z. Yang, X. Liu, Y. Deng, Forward modeling of solar coronal magnetic-field measurements based on a magnetic-field-induced transition in Fe X. *Astrophys. J.* **920**, 116 (2021). doi:10.3847/1538-4357/ac1792

15. V. M. Nakariakov, L. Ofman, Determination of the coronal magnetic field by coronal loop oscillations. *Astron. Astrophys.* **372**, L53–L56 (2001). doi:10.1051/0004-6361:20010607

16. D. B. Jess, V. E. Reznikova, R. S. I. Ryans, D. J. Christian, P. H. Keys, M. Mathioudakis, D. H. Mackay, S. Krishna Prasad, D. Banerjee, S. D. T. Grant, S. Yau, C. Diamond, Solar coronal magnetic fields derived using seismology techniques applied to omnipresent sunspot waves. *Nat. Phys.* **12**, 179–185 (2015). doi:10.1038/nphys3544

17. R. J. Morton, S. Tomczyk, R. Pinto, Investigating Alfvénic wave propagation in coronal open-field regions. *Nat. Commun.* **6**, 7813 (2015). doi:10.1038/ncomms8813 Medline

18. S. Tomczyk, S. W. McIntosh, S. L. Keil, P. G. Judge, T. Schad, D. H. Seeley, J. Edmondson, Alfven waves in the solar corona. *Science* **317**, 1192–1196 (2007). doi:10.1126/science.1143304 Medline

19. R. J. Morton, M. J. Weberg, J. A. McLaughlin, A basal contribution from *p*-modes to the Alfvénic wave flux in the Sun's corona. *Nat. Astron.* **3**, 223–229 (2019). doi:10.1038/s41550-018-0668-9

20. S. Tomczyk, G. L. Card, T. Darnell, D. F. Elmore, R. Lull, P. G. Nelson, K. V. Streander, J. Burkepile, R. Casini, P. G. Judge, An instrument to measure coronal emission line polarization. *Sol. Phys.* **247**, 411–428 (2008). doi:10.1007/s11207-007-9103-6

21. Z. Yang, C. Bethge, H. Tian, S. Tomczyk, R. Morton, G. Del Zanna, S. W. McIntosh, B. B. Karak, S. Gibson, T. Samanta, J. He, Y. Chen, L. Wang, Global maps of the magnetic field in the solar corona. *Science* **369**, 694–697 (2020). doi:10.1126/science.abb4462 Medline

22. Z. Yang, H. Tian, S. Tomczyk, R. Morton, X. Y. Bai, T. Samanta, Y. J. Chen, Mapping the magnetic field in the solar corona through magnetoseismology. *Sci. China Technol. Sci.* **63**, 2357–2368 (2020). doi:10.1007/s11431-020-1706-9

23. E. Landi, S. R. Habbal, S. Tomczyk, Coronal plasma diagnostics from ground-based observations. *J. Geophys. Res. Space Phys.* **121**, 8237–8249 (2016). doi:10.1002/2016JA022598

24. H. Tian, S. Tomczyk, S. W. McIntosh, C. Bethge, G. de Toma, S. Gibson, Observations of coronal mass ejections with the Coronal Multichannel Polarimeter. *Sol. Phys.* **288**, 637–650 (2013). doi:10.1007/s11207-013-0317-5

25. Materials and methods are available as supplementary materials.

26. S. Tomczyk, S. W. McIntosh, Time-distance seismology of the solar corona with CoMP. *Astrophys. J.* **697**, 1384–1391 (2009). doi:10.1088/0004-637X/697/2/1384

27. N. Magyar, T. Van Doorsselaere, Assessing the capabilities of dynamic coronal seismology of Alfvénic waves through forward modeling. *Astrophys. J.* **856**, 144 (2018). doi:10.3847/1538-4357/aab42c

28. J. M. Darnel, D. B. Seaton, C. Bethge, L. Rachmeler, A. Jarvis, S. M. Hill, C. L. Peck, J. M. Hughes, J. Shapiro, A. Riley, G. Vasudevan, L. Shing, G. Koener, C. Edwards, D. Mathur, S. Timothy, The GOES-R Solar UltraViolet Imager. *Space Weather* **20**, e2022SW003044 (2022). doi:10.1029/2022SW003044

29. D. H. Hathaway, The Solar Cycle. *Living Rev. Sol. Phys.* **12**, 4 (2015). doi:10.1007/lrsp-2015-4 Medline

30. P. H. Scherrer, J. Schou, R. I. Bush, A. G. Kosovichev, R. S. Bogart, J. T. Hoeksema, Y. Liu, T. L. Duvall Jr., J. Zhao, A. M. Title, C. J. Schrijver, T. D. Tarbell, S. Tomczyk, The *Helioseismic and Magnetic Imager* (HMI) investigation for the *Solar Dynamics Observatory* (SDO). *Sol. Phys.* **275**, 207–227 (2012). doi:10.1007/s11207-011-9834-2

31. V. Bumba, R. Howard, Solar activity and recurrences in magnetic-field distribution. *Sol. Phys.* **7**, 28–38 (1969). doi:10.1007/BF00148402

32. L. van Driel-Gesztelyi, L. M. Green, Evolution of Active Regions. *Living Rev. Sol. Phys.* **12**, 1 (2015). doi:10.1007/lrsp-2015-1

33. Z. Mikić, C. Downs, J. A. Linker, R. M. Caplan, D. H. Mackay, L. A. Upton, P. Riley, R. Lionello, T. Török, V. S. Titov, J. Wijaya, M. Druckmüller, J. M. Pasachoff, W. Carlos, Predicting the corona for the 21 August 2017 total solar eclipse. *Nat. Astron.* **2**, 913–921 (2018). doi:10.1038/s41550-018-0562-5

34. R. Lionello, J. A. Linker, Z. Mikić, Multispectral emission of the Sun during the first Whole Sun Month: Magnetohydrodynamic Simulations. *Astrophys. J.* **690**, 902–912 (2009). doi:10.1088/0004-637X/690/1/902

35. C. Downs, Associated modeling data & materials for manuscript: Observing the evolution of the Sun's global coronal magnetic field over eight months, Data set, Zenodo (2024); https://doi.org/10.5281/zenodo.13351573.

36. Z. Yang, Analysis codes for UCoMP coronal magnetic field measurement paper, Zenodo (2024); https://doi.org/10.5281/zenodo.13367069.

37. MAS: A Model of the Solar Corona and Inner Heliosphere (Predictive Science); https://www.predsci.com/corona/model_desc.html.

38. T. A. Schad, J. R. Kuhn, A. Fehlmann, I. F. Scholl, D. Harrington, T. Rimmele, A. Tritschler, First Infrared Coronal Spectra from DKIST/Cryo-NIRSP: Comparisons with Global MHD Models. *Astrophys. J.* **943**, 59 (2023). doi:10.3847/1538-4357/acabbd

39. P. H. Scherrer, R. S. Bogart, R. I. Bush, J. T. Hoeksema, A. G. Kosovichev, J. Schou, W. Rosenberg, L. Springer, T. D. Tarbell, A. Title, C. J. Wolfson, I. Zayer, The MDI Engineering Team, The solar oscillations investigation – Michelson Doppler Imager. *Sol. Phys.* **162**, 129–188 (1995). doi:10.1007/BF00733429

40. Y. Liu, J. T. Hoeksema, P. H. Scherrer, J. Schou, S. Couvidat, R. I. Bush, T. L. Duvall Jr., K. Hayashi, X. Sun, X. Zhao, Comparison of line-of-sight magnetograms taken by the *Solar Dynamics Observatory/Helioseimic and Magnetic Imager* and *Solar and Heliospheric*

Observatory/Michelson Doppler Imager. *Sol. Phys.* **279**, 295–316 (2012). doi:10.1007/s11207-012-9976-x

41. K. P. Dere, E. Landi, H. E. Mason, B. C. Monsignori Fossi, P. R. Young, CHIANTI – An atomic database for emission lines. I. Wavelengths greater than 50 Å. *Astron. Astrophys. Suppl. Ser.* **125**, 149–173 (1997). doi:10.1051/aas:1997368

42. G. Del Zanna, K. P. Dere, P. R. Young, E. Landi, CHIANTI—An Atomic Database for Emission Lines. XVI. Version 10, Further Extensions. *Astrophys. J.* **909**, 38 (2021). doi:10.3847/1538-4357/abd8ce

43. G. Del Zanna, P. J. Storey, Atomic data for astrophysics: Fe XIII soft X-ray lines. *Astron. Astrophys.* **543**, A144 (2012). doi:10.1051/0004-6361/201219193

44. S. E. Gibson, T. A. Kucera, S. M. White, J. B. Dove, Y. Fan, B. C. Forland, L. A. Rachmeler, C. Downs, K. K. Reeves, FORWARD: A toolset for multiwavelength coronal magnetometry. *Front. Astron. Space Sci.* **3**, 8 (2016). doi:10.3389/fspas.2016.00008

45. M. S. Ruderman, R. Erdélyi, Transverse Oscillations of Coronal Loops. *Space Sci. Rev.* **149**, 199–228 (2009). doi:10.1007/s11214-009-9535-4

46. D. M. Long, G. Valori, D. Pérez-Suárez, R. J. Morton, A. M. Vásquez, Measuring the magnetic field of a trans-equatorial loop system using coronal seismology. *Astron. Astrophys.* **603**, A101 (2017). doi:10.1051/0004-6361/201730413

47. H. Peter, S. Bingert, J. A. Klimchuk, C. de Forest, J. W. Cirtain, L. Golub, A. R. Winebarger, K. Kobayashi, K. E. Korreck, Structure of solar coronal loops: From miniature to large-scale. *Astron. Astrophys.* **556**, A104 (2013). doi:10.1051/0004-6361/201321826

48. P. G. Judge, Spectral Lines for Polarization Measurements of the Coronal Magnetic Field. I. Theoretical Intensities. *Astrophys. J.* **500**, 1009–1022 (1998). doi:10.1086/305775

49. I. De Moortel, D. J. Pascoe, Putting Coronal Seismology Estimates of the Magnetic Field Strength to the Test. *Astrophys. J.* **699**, L72–L75 (2009). doi:10.1088/0004-637X/699/2/L72

50. V. M. Nakariakov, D. Y. Kolotkov, Magnetohydrodynamic Waves in the Solar Corona. *Annu. Rev. Astron. Astrophys.* **58**, 441–481 (2020). doi:10.1146/annurev-astro-032320-042940

51. J. Dudík, G. Del Zanna, J. Rybák, J. Lörinčík, E. Dzifčáková, H. E. Mason, S. Tomczyk, M. Galloy, Electron Densities in the Solar Corona Measured Simultaneously in the Extreme Ultraviolet and Infrared. *Astrophys. J.* **906**, 118 (2021). doi:10.3847/1538-4357/abcd91

52. D. R. Flower, G. Pineau de Forêts, Excitation of the Fe XIII Spectrum in the Solar Corona. *Astron. Astrophys.* **24**, 181–192 (1973).

53. R. Sharma, R. J. Morton, Transverse energy injection scales at the base of the solar corona. *Nat. Astron.* **7**, 1301–1308 (2023). doi:10.1038/s41550-023-02070-1

54. M. S. Ruderman, M. Goossens, J. Andries, Nonlinear propagating kink waves in thin magnetic tubes. *Phys. Plasmas* **17**, 082108 (2010). doi:10.1063/1.3464464

55. N. Magyar, T. Van Doorsselaere, Damping of nonlinear standing kink oscillations: A numerical study. *Astron. Astrophys.* **595**, A81 (2016). doi:10.1051/0004-6361/201629010

56. R. J. Morton, A. K. Tiwari, T. Van Doorsselaere, J. A. McLaughlin, Weak Damping of Propagating MHD Kink Waves in the Quiescent Corona. *Astrophys. J.* **923**, 225 (2021). doi:10.3847/1538-4357/ac324d

57. M. J. Aschwanden, C. J. Schrijver, Coronal Loop Oscillations Observed with Atmospheric Imaging Assembly—Kink Mode with Cross-Sectional and Density Oscillations. *Astrophys. J.* **736**, 102 (2011). doi:10.1088/0004-637X/736/2/102

58. L. Ofman, M. Parisi, A. K. Srivastava, Three-dimensional MHD modeling of vertical kink oscillations in an active region plasma curtain. *Astron. Astrophys.* **582**, A75 (2015). doi:10.1051/0004-6361/201425054

59. F. Chen, H. Peter, Using coronal seismology to estimate the magnetic field strength in a realistic coronal model. *Astron. Astrophys.* **581**, A137 (2015). doi:10.1051/0004-6361/201526237

60. T. Van Doorsselaere, A. Debosscher, J. Andries, S. Poedts, The effect of curvature on quasi-modes in coronal loops. *Astron. Astrophys.* **424**, 1065–1074 (2004). doi:10.1051/0004-6361:20041239

61. M. Guo, T. Van Doorsselaere, B. Li, M. Goossens, Horizontally and vertically polarized kink oscillations in curved solar coronal loops. *Astron. Astrophys.* **687**, A30 (2024). doi:10.1051/0004-6361/202449991

62. L. Ofman, Three-Dimensional Magnetohydrodynamic Models of Twisted Multithreaded Coronal Loop Oscillations. *Astrophys. J.* **694**, 502–511 (2009). doi:10.1088/0004-637X/694/1/502

63. T. Van Doorsselaere, M. S. Ruderman, D. Robertson, Transverse oscillations of two parallel coronal loops. *Astron. Astrophys.* **485**, 849–857 (2008). doi:10.1051/0004-6361:200809841

64. M. Luna, J. Terradas, R. Oliver, J. L. Ballester, Transverse oscillations of two coronal loops. *Astrophys. J.* **676**, 717–727 (2008). doi:10.1086/528367

65. S. W. McIntosh, B. De Pontieu, S. Tomczyk, A Coherence-Based Approach for Tracking Waves in the Solar Corona. *Sol. Phys.* **252**, 321–348 (2008). doi:10.1007/s11207-008-9257-x

66. NSO/GONG Farside Archives (National Solar Observatory); https://farside.nso.edu/archive.html.

67. C. Lindsey, D. C. Braun, Helioseismic Holography. *Astrophys. J.* **485**, 895–903 (1997). doi:10.1086/304445

68. I. González Hernández, F. Hill, C. Lindsey, Calibration of Seismic Signatures of Active Regions on the Far Side of the Sun. *Astrophys. J.* **669**, 1382–1389 (2007). doi:10.1086/521592

69. G. J. D. Petrie, Solar Magnetism in the Polar Regions. *Living Rev. Sol. Phys.* **12**, 5 (2015). doi:10.1007/lrsp-2015-5